



Exploring the Complex Ionization Environment of the Turbulent DM Tau Disk

Deryl E. Long¹ , L. Ilsedore Cleeves¹ , Fred C. Adams² , Sean Andrews³ , Edwin A. Bergin⁴ , Viviana V. Guzmán⁵ , Jane Huang⁶ , A. Meredith Hughes⁷ , Chunhua Qi³ , Kamber Schwarz⁸ , Jacob B. Simon⁹ , and David Wilner³

¹ University of Virginia, 530 McCormick Rd., Charlottesville, VA 22903, USA

² Physics Department, University of Michigan, Ann Arbor, MI 48109, USA

³ Harvard-Smithsonian Center for Astrophysics, 60 Garden St., Cambridge, MA 02138, USA

⁴ Department of Astronomy, University of Michigan, 1085 South University Avenue, Ann Arbor, MI 48109, USA

⁵ Instituto de Astrofísica, Pontificia Universidad Católica de Chile, Av. Vicuña Mackenna 4860, 7820436 Macul, Santiago, Chile

⁶ Columbia University, 538 West 120th Street, New York, NY 10027, USA

⁷ Van Vleck Observatory, Wesleyan University, 96 Foss Hill Dr., Middletown, CT 06459, USA

⁸ Max Planck Institute for Astronomy, Königstuhl 17, Heidelberg, Germany

⁹ Department of Physics and Astronomy, Iowa State University, Ames, IA 50010, USA

Received 2024 January 26; revised 2024 June 21; accepted 2024 June 25; published 2024 August 27

Abstract

Ionization drives important chemical and dynamical processes within protoplanetary disks, including the formation of organics and water in the cold midplane and the transportation of material via accretion and magnetohydrodynamic flows. Understanding these ionization-driven processes is crucial for understanding disk evolution and planet formation. We use new and archival Atacama Large Millimeter/submillimeter Array observations of HCO^+ , H^{13}CO^+ , and N_2H^+ to produce the first forward-modeled 2D ionization constraints for the DM Tau protoplanetary disk. We include ionization from multiple sources and explore the disk chemistry under a range of ionizing conditions. Abundances from our 2D chemical models are postprocessed using non-LTE radiative transfer, visibility sampling, and imaging, and are compared directly to the observed radial emission profiles. The observations are best fit by a modestly reduced cosmic-ray ionization rate ($\zeta_{\text{CR}} \sim 10^{-18} \text{ s}^{-1}$) and a hard X-ray spectrum (hardness ratio = 0.3), which we associate with stellar flaring conditions. Our best-fit model underproduces emission in the inner disk, suggesting that there may be an additional mechanism enhancing ionization in DM Tau's inner disk. Overall, our findings highlight the complexity of ionization in protoplanetary disks and the need for high-resolution multiline studies.

Unified Astronomy Thesaurus concepts: [Protoplanetary disks \(1300\)](#); [Planet formation \(1241\)](#); [Circumstellar disks \(235\)](#); [Astrochemistry \(75\)](#)

1. Introduction

Ionization plays a critical role in the evolution of protoplanetary disks and the formation of planets within these environments. Ions drive the most rapid chemical reactions (Herbst & Klemperer 1973; Tielens & Hagen 1982) in the coldest regions of the disk where neutral-neutral reactions are less efficient. Ionization also impacts the redistribution of planet-forming materials by driving transport via accretion and magnetohydrodynamic flows. Sufficient ionization allows the gas to couple to magnetic field lines, and in turn drives a disk wind (Blandford & Payne 1982) and/or the magneto-rotational instability (MRI; Balbus & Hawley 1991). Ionization is also a key input parameter for chemical models, the results of which are used to interpret observations of disks and in turn predict the compositions of forming planets (Eistrup et al. 2018; Price et al. 2020).

Ions are responsible for driving chemical complexity in the cold ($T < 50$ K) disk midplane, creating formation pathways for organics (Cleeves et al. 2016) and water (van Dishoeck et al. 2013). If disks cannot efficiently form water, nascent planets would have to rely solely on inherited water from the parent molecular cloud (Cleeves et al. 2014). The efficiency of cold-water production may also vary with distance from the star, which would result in variations in ice across the disk.

Understanding the distribution of ice is important, as the habitability of Earth-like planets may depend on postformation delivery of water ice from asteroids and comets. The distribution of ice also influences the atmospheric and core compositions of gas giants (Öberg et al. 2011; Miotello et al. 2023).

Ionization is also an important parameter for constraining hydro- and magnetohydrodynamic processes that impact the evolution of planet-forming material within the disk. In well-ionized regions of the disk, turbulence is thought to be primarily driven by the MRI. In weakly ionized regions of the disk, turbulence may be present, but its strength and nature (e.g., degree of isotropy) will be modified by nonideal effects, such as ohmic diffusion (Fleming & Stone 2003; Gole et al. 2016), ambipolar diffusion (Simon et al. 2013a, 2013b), and the Hall effect (Bai 2015; Simon et al. 2015). Moreover, recent modeling studies that consider nonideal effects suggest that the accretion flow in the inner disk is largely laminar and that accretion heating is much weaker than previously assumed (Mori et al. 2019). If ionization is low enough, then hydrodynamic instabilities such as the vertical shear instability (or VSI; Nelson et al. 2013), convective overstability (or COS; Klahr & Hubbard 2014), and the zombie vortex instability (or ZVI; Marcus et al. 2015) affect the gas dynamics in a very different manner than do the magnetic effects (see, e.g., Nelson et al. 2013; Melon Fuksman et al. 2024). The gas flows driven by these various processes impact the conditions for planet formation.

For planets to form, micron-sized dust grains must stick together to form aggregates and eventually planetesimals on



Original content from this work may be used under the terms of the [Creative Commons Attribution 4.0 licence](#). Any further distribution of this work must maintain attribution to the author(s) and the title of the work, journal citation and DOI.

size scales of ~ 0.1 – 100 km. Several complications must be overcome in this process, including radial drift (Whipple 1972) and fragmentation (Blum 2018). The “streaming instability” is a promising mechanism for overcoming dust growth barriers, as dense collections of dust are able to form planetesimals via direct gravitational collapse (Youdin & Goodman 2005), although this mechanism can be suppressed by background turbulence if present (Chen & Lin 2020; Gole et al. 2020; Umurhan et al. 2020; Lim et al. 2023; but see Johansen et al. 2007; Yang et al. 2018). Thus, the ionization state of the disk gas can influence the overall turbulence, which can have attendant effects on planet formation.

Ionization in disks is driven by several sources including UV photons, X-rays, and cosmic rays (CRs). Each of these sources ionize different vertical and radial regions of the disk. UV photons drive ionization at the disk surface but are quickly attenuated at depths greater than 10^{-3} g cm $^{-2}$ (Bergin et al. 2007). X-rays are able to travel deeper into the disk, reaching depths from $\sim 10^{-2}$ g cm $^{-2}$ for soft X-rays (1 keV) to 1.6 g cm $^{-2}$ for hard X-rays (10 keV). Thus, X-rays may have a significant impact in dense layers depending on the hardness of the stellar spectrum (Igea & Glassgold 1999). CRs are able to ionize gas column densities up to ~ 100 g cm $^{-2}$, and are thus expected to be the most important sources of ionization in the most dense and cold regions of the disk where X-rays are strongly attenuated.

The rate of CR ionization in the dense interstellar medium (ISM) is on the order of 10^{-17} s $^{-1}$, but this rate could be reduced by orders of magnitude due to CR exclusion by stellar winds or magnetic fields (Cleeves et al. 2013, 2015) or enhanced due to local particle acceleration (Padovani et al. 2015, 2016). Within the disk itself, detouring of CRs along sheared magnetic field lines can increase the effective column density by up to 2 orders of magnitude and reduce the rate of CR ionization in the disk midplane (Fujii & Kimura 2022). Stars forming in clusters may be exposed to even stronger external radiation via CRs as well as external X-rays and UV photons (Clarke 2007; Adams 2010). Recent observations of molecular ions in disks and protostars reveal evidence of spatial variation in ionization rates, possibly linked to the processes outlined above (Aikawa et al. 2021; Seifert et al. 2021; Cabedo et al. 2023). Ultimately, navigating the complex picture of ionization across the 2D disk environment requires a merging of detailed dynamical and chemical models with reliable observational constraints.

In this work, we constrain the radially resolved ionization structure of the DM Tau protoplanetary disk using HCO $^+$, H 13 CO $^+$, and N $_2$ H $^+$. DM Tau is a large (gas disk radius ~ 800 au; Dartois et al. 2003), well-studied disk around a $0.54 M_\odot$ T Tauri star (Simon et al. 2000). DM Tau is one of only two disks in which turbulence has been measured (Flaherty et al. 2020, 2024), and it has yet to be determined whether this turbulence is ionization driven via magnetic effects, such as the MRI. Previous work suggests that DM Tau’s disk is well ionized in the warm molecular layer ($x_e \sim 10^{-7}$; Teague et al. 2015) with the ionization fraction decreasing toward the midplane (Öberg et al. 2011), consistent with theoretical expectations. We present new Atacama Large Millimeter/submillimeter Array (ALMA) observations of molecular ions in DM Tau and use an updated physical model and 2D chemical model to explore the role of different ionization sources (namely CRs and X-rays) in driving ionization in DM Tau. We also discuss the usefulness of the different molecular lines for studying ionization in this disk and what they tell us, individually and in concert.

2. Atacama Large Millimeter/submillimeter Array Observations

Observations of HCO $^+ J = 4-3$, N $_2$ H $^+ J = 4-3$, and H 13 CO $^+ J = 3-2$ were taken with ALMA under project code 2019.1.00379.S (PI: Cleeves). We also made use of data from project 2015.1.00678.S (PI: Qi) to constrain N $_2$ H $^+ J = 3-2$. A detailed description of those observations and their calibration can be found in Qi et al. (2019). The Band 7 HCO $^+ J = 4-3$ and N $_2$ H $^+ J = 4-3$ data were taken on 2019 October 17–18 with 43 antennas covering 15–740 m baselines. These data were calibrated with the CASA pipeline, with J0423–0120 as the bandpass calibrator and J0510+1800 as the phase calibrator. The Band 6 H 13 CO $^+ J = 3-2$ data were taken on 2021 July 7 with 43 antennas covering 14–2492 m baselines.

For the H 13 CO $^+$ data set, we saw no improvement in the continuum rms with phase self-calibration, so the data were calibrated only with the standard pipeline and subsequently imaged. For the data set with HCO $^+ J = 4-3$ and N $_2$ H $^+ J = 4-3$, we applied one round of phase self-calibration, which resulted in a small factor of $1.1 \times$ improvement in the rms of the continuum data. We performed continuum subtraction and imaging for all lines using the `uvcontsub` and `tclean` commands from CASA v5.6.1 and Keplerian masks generated with the `keplerian_mask` Python package (Teague 2020).¹⁰ The masks for both N $_2$ H $^+$ lines contain three components to capture the hyperfine emission structures. For the line imaging of HCO $^+$, we used Briggs weighting and a robustness parameter of 0.5. For H 13 CO $^+$ and N $_2$ H $^+ J = 4-3$, we used natural weighting and a `uvtaper` of 0''.5 to maximize sensitivity. Following Qi et al. (2019), we imaged N $_2$ H $^+ J = 3-2$ using natural weighting.

The data for N $_2$ H $^+ J = 4-3$ were significantly more noisy than the other lines due to their close proximity to atmospheric water-vapor features. We used the `matched_filter` command from the `VISIBLE` Python package (Loomis et al. 2018) with our HCO $^+$ detection as a filter.¹¹ We saw a 6σ response, indicating the presence of N $_2$ H $^+ J = 4-3$. Though the N $_2$ H $^+ J = 4-3$ line is not resolved in the observations, we still report the integrated flux and include this line in our analysis. Channel maps for the three resolved line detections are shown in Figure 1 and additional information about the line and continuum observations is listed in Table 1. We create velocity-integrated intensity (zeroth-moment) maps (Figure 2) for the resolved detections using the `bettermoments` Python package (Teague & Foreman-Mackey 2018).¹² We report the rms measured in line-free channels. We produce radial line intensity profiles using the `GoFish` Python package (Teague 2019) and discuss these in more detail in Section 4.¹³

3. Modeling DM Tau

3.1. Physical Model

Our physical model combines a well-constrained gas density and temperature structure from Flaherty et al. (2020) with a dust structure based on continuum visibilities and spectral energy distribution (SED) fitting presented in Andrews et al. (2011). The gas density and temperature

¹⁰ https://github.com/richteague/keplerian_mask

¹¹ <https://github.com/AstroChem/VISIBLE>

¹² <https://github.com/richteague/bettermoments>

¹³ <https://github.com/richteague/gofish>

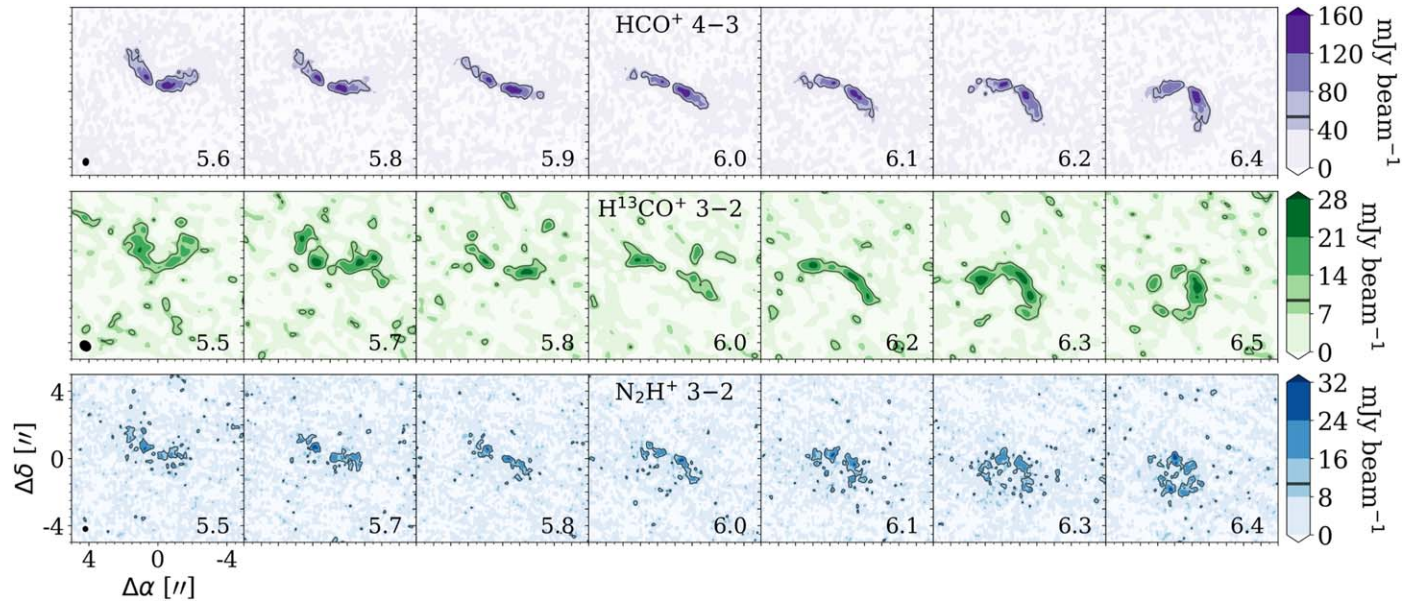


Figure 1. Channel maps for $\text{HCO}^+ J = 4-3$, $\text{H}^{13}\text{CO}^+ J = 3-2$, and $\text{N}_2\text{H}^+ J = 3-2$. The solid contour represents 3σ . The beam is illustrated in the bottom-left corner, and the velocity relative to the local standard of rest in kilometers per second is indicated in the bottom-right corner of each channel.

Table 1
Line and Continuum Observations

| Transition | Rest Freq. (GHz) | Beam (PA) | Channel Width (km s ⁻¹) | rms (mJy beam ⁻¹) | Integrated Flux ^a (Jy km s ⁻¹) |
|------------------------------------|---------------------|--|--|----------------------------------|--|
| $\text{N}_2\text{H}^+ J = 4-3$ | 372.672 | $0.^{\circ}66 \times 0.^{\circ}64$ (7.0°) | 0.114 | 46 | 0.7 ± 0.24 |
| $\text{HCO}^+ J = 4-3$ | 356.734 | $0.^{\circ}42 \times 0.^{\circ}32$ (-6.2°) | 0.119 | 8.6 | 6.8 ± 0.69 |
| $\text{N}_2\text{H}^+ J = 3-2$ | 279.512 | $0.^{\circ}29 \times 0.^{\circ}27$ (0.99°) | 0.150 | 3.9 | 1.3 ± 0.14 |
| $\text{H}^{13}\text{CO}^+ J = 3-2$ | 260.255 | $0.^{\circ}67 \times 0.^{\circ}55$ (46°) | 0.163 | 3.2 | 0.41 ± 0.046 |
| Continuum | 1 mm | $0.^{\circ}25 \times 0.^{\circ}16$ (53°) | 1875 MHz ^b | 0.15 | 0.08 ± 0.008 Jy |
| Continuum | 1.3 mm | $0.^{\circ}38 \times 0.^{\circ}28$ (-17°) | 1875 MHz | 0.27 | 0.16 ± 0.016 Jy |

Notes.

^a The disk-integrated flux was measured within the same Keplerian masks used for imaging. Errors were estimated by applying the mask to line-free channels and include the nominal 10% flux calibration uncertainty from ALMA.

^b Bandwidth.

structures were parameterized and fit using the Markov chain Monte Carlo (MCMC) routine `emcee` (Foreman-Mackey et al. 2013) and high-resolution CO observations. A detailed description of the CO modeling and temperature parameterization can be found in Flaherty et al. (2020). The dust structure is derived from the azimuthally symmetric gas surface density profile:

$$\Sigma_g = \Sigma_c \left(\frac{R}{R_c} \right)^{-\gamma} \exp \left[- \left(\frac{R}{R_c} \right)^{2-\gamma} \right], \quad (1)$$

where the characteristic scaling radius $R_c = 135$ au was determined by Andrews et al. (2011) and the surface density gradient is set to $\gamma = 1$. Our model assumes a global dust-to-gas ratio of $\xi = 0.01$. The dust disk has a flared vertical structure with a scale height distribution given by

$$H(r) = H_{100} \left(\frac{r}{100 \text{ au}} \right)^\psi, \quad (2)$$

where $H_{100} = 9.75$ au and $\psi = 1.2$. Following the SED fitting results in Andrews et al. (2011), we account for the disk's inner

gap by depleting the dust by a factor $\delta_{\text{cav}} = 4.8$ in the region $R < R_{\text{cav}} = 19$ au. With the resulting surface density profile, we calculate dust densities for small (0.005 – 1 μm) and large (0.005 μm – 1 mm) grains using the density distributions

$$\rho_s = \frac{(1-f)\Sigma_d}{\sqrt{2\pi}H} \exp \left[-\frac{1}{2} \left(\frac{z}{H} \right)^2 \right] \quad (3)$$

and

$$\rho_l = \frac{f\Sigma_d}{\sqrt{2\pi}H\chi} \exp \left[-\frac{1}{2} \left(\frac{z}{\chi H} \right)^2 \right], \quad (4)$$

where f and χ are settling parameters, fixed at 0.85 and 0.2, respectively, meaning that large grains make up 85% of the total dust column and are distributed up to 20% of the disk scale height. Both the small and large dust grain populations follow an MRN size distribution (Mathis et al. 1977) within their respective size ranges. The distribution of gas, large dust grains, small dust grains, and temperature structure are shown in Figure 3.

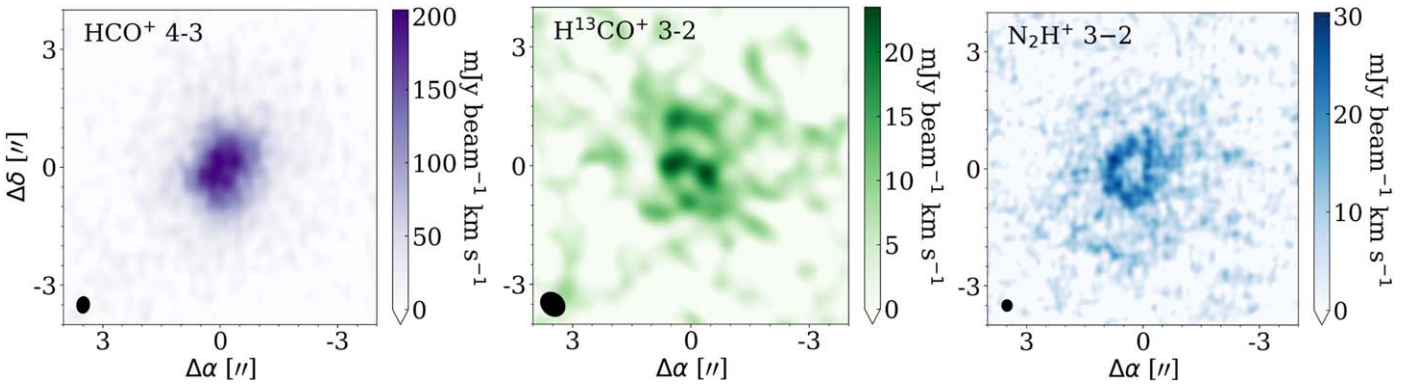


Figure 2. Integrated intensity (moment-zero) maps for the resolved observations of $\text{HCO}^+ J = 4-3$, $\text{H}^{13}\text{CO}^+ J = 3-2$, and $\text{N}_2\text{H}^+ J = 3-2$. The beam is illustrated in the bottom-left corner. Moment-zero maps were produced using the `bettermoments` (Teague & Foreman-Mackey 2018) Python package.

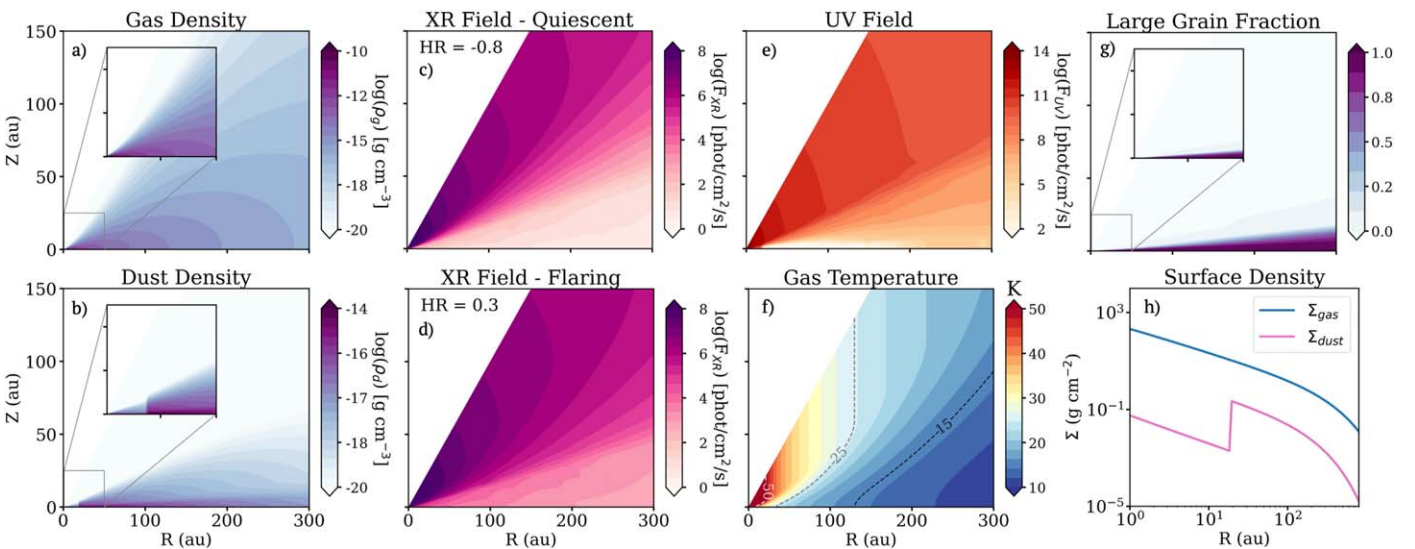


Figure 3. Panel (a) shows the gas densities from Flaherty et al. (2020) and panel (b) shows the total dust density including both small and large grains. Panels (c) and (d) show the integrated X-ray flux from 1–20 keV for the quiescent and flaring X-ray models. Panel (e) shows the wavelength-integrated UV flux and panel (f) shows the gas temperature structure with 50 K, 25 K, and 15 K contours. Panel (g) shows the fraction of large grains in the disk, which are concentrated in the disk midplane. Panel (h) shows the surface density profiles for our gas and dust models.

3.2. Ionization Model

Our models include ionization from three sources: UV photons, X-ray photons, and CRs. We exclude effects of inherited short-lived radionuclides (SLRs) for now since their initial abundance is uncertain and any inherited SLRs' rate of ionization will have decayed over DM Tau's estimated lifetime of $\sim 3\text{--}7$ Myr (Simon et al. 2000), and ultimately should have negligible contributions to bulk disk ionization at the disk's current age.

Two-dimensional stellar X-ray and UV fluxes (Figure 3) were obtained using the Bethell & Bergin (2011) Monte Carlo radiative transfer code and cross sections. We use an observed stellar UV spectrum for TW Hya and scale it to DM Tau's far-UV luminosity by a factor of 2.16. We explore the effects of both quiescent and “flaring” X-ray (or XR) states using template spectra from Cleeves et al. (2015). Both spectra are scaled to an X-ray luminosity of $2.5 \times 10^{29} \text{ erg s}^{-1}$ for DM Tau, which is a factor of ~ 2 below the upper limit of $4.6 \times 10^{29} \text{ erg s}^{-1}$ from Damiani et al. (1995) after excluding energies < 1 keV. Our X-ray models include energies from 1–20 keV. The quiescent and flaring states are distinguished by

their respective hardness ratios ($\text{HR} = (L_{\text{soft}} - L_{\text{hard}})/(L_{\text{soft}} + L_{\text{hard}})$). The quiescent model ($\text{HR} = -0.8$) is soft X-ray dominated, while the hardened “flaring” model ($\text{HR} = 0.3$) is hard X-ray dominated. Panels (c) and (d) in Figure 3 demonstrate the resulting difference in flux between the two XR models.

Our modeling suite includes five different incident CR ionization rates (ζ_{CR}) listed in Table 2 and CR attenuation as a function of column density, as described in Cleeves et al. (2013). Our two highest CR rates, M02 and W98, represent two different estimates of the local interstellar CR spectrum. The Moskalenko et al. (2002) spectrum is the best-fit model based on the diffuse gamma-ray background as well as other data including the proton, antiproton, and alpha-particle spectra. The rate from Webber (1998) approximates the conditions of the dense ISM based on measurements taken by Voyager and Pioneer. The solar system minimum modulation (SSM) and maximum modulation (SSX) are based on measured CR rates on Earth, representing the CR ionization for our solar system given minimum and maximum amounts of CR modulation via stellar winds. Our lowest CR rate is the T Tauri maximum modulation (TTX), which was extrapolated by

Table 2
CR Ionization Rates (ζ_{CR}) Used for Our Modeling Suite

| Cosmic-ray Model | Label | ζ_{CR} |
|--------------------------|-------|-----------------------|
| Moskalenko et al. (2002) | M02 | 6.8×10^{-16} |
| Webber (1998) | W98 | 2.0×10^{-17} |
| Solar System Min. Mod. | SSM | 1.1×10^{-18} |
| Solar System Max. Mod. | SSX | 1.6×10^{-19} |
| T Tauri Max. Mod. | TTX | 1.0×10^{-21} |

Note. Here “Min. Mod.” and “Max. Mod.” refer to the efficiency of modulation by stellar winds (Cleeves et al. 2013). In addition to the five ζ_{CR} values listed here, we also model two different X-ray conditions, yielding a modeling suite with a total of 10 models.

Table 3
Model Initial Abundances Relative to Total Hydrogen Density

| Molecule | Abundance | Molecule | Abundance |
|----------------------|------------------------|-----------------------------|------------------------|
| H ₂ | 5.00×10^{-1} | He | 1.40×10^{-1} |
| N ₂ | 3.75×10^{-5} | HCN | 1.00×10^{-8} |
| CS | 4.00×10^{-9} | SO | 5.00×10^{-9} |
| HCO ⁺ | 9.00×10^{-9} | H ₃ ⁺ | 1.00×10^{-8} |
| C ₂ H | 8.00×10^{-9} | CO | 2.60×10^{-5} |
| H ₂ O(gr) | 1.00×10^{-4} | Si ⁺ | 1.00×10^{-11} |
| Mg ⁺ | 1.00×10^{-11} | Fe ⁺ | 1.00×10^{-11} |
| Grains | 6.00×10^{-12} | ... | ... |

Note. The (gr) suffix indicates that the species is initialized on grains instead of in the gas phase. The elemental abundances for the dominant molecules N, C, and O are 7.5×10^{-5} , 5×10^{-5} , and 2.5×10^{-4} , respectively.

Cleeves et al. (2013) to account for enhanced CR modulation by the higher stellar wind outflow rates measured for T Tauri stars. Additional details for the CR rates can be found in Cleeves et al. (2013).

3.3. Chemical Model

Chemical abundances are calculated as a function of position and time using a 2D time-dependent rate equation chemical code from Fogel et al. (2011) adapted in Cleeves et al. (2014) and Anderson et al. (2021). The results presented in this work utilize our latest updated chemical network with 18,608 reactions and 1038 species, including deuterium isotopologues. Our network does not include carbon isotopes ¹²C and ¹³C, so we retrieve H¹³CO⁺ abundances by applying a constant ¹²C/¹³C ratio of 60 (Langer & Penzias 1993). However, in reality we expect that the gas-phase ¹²C/¹³C ratio may have radial variations, particularly across the CO snowline (Yoshida et al. 2022). Our initial abundances (Table 3) are representative of the chemical conditions in a typical molecular cloud. Yet it has been shown that DM Tau’s CO depletion ranges from a factor of 1–10 radially across the disk (Zhang et al. 2019). Based on this range, we choose to use an “average” CO depletion factor of 5 such that our starting CO abundance is 2.6×10^{-5} . We do not aim to determine if the CO destruction in DM Tau occurs within the lifetime of the disk or prior (e.g., Bergner et al. 2020), but rather aim to create a chemical environment reflective of DM Tau’s present state.

We run a grid of models using the physical structure and radiation fields shown in Figure 3. With five different CR ionization rates and two XR fields, we have a total of 10 models. Models are computed out to a time of 1 Myr, at which point the ion chemistry has settled into a pseudo-steady state.

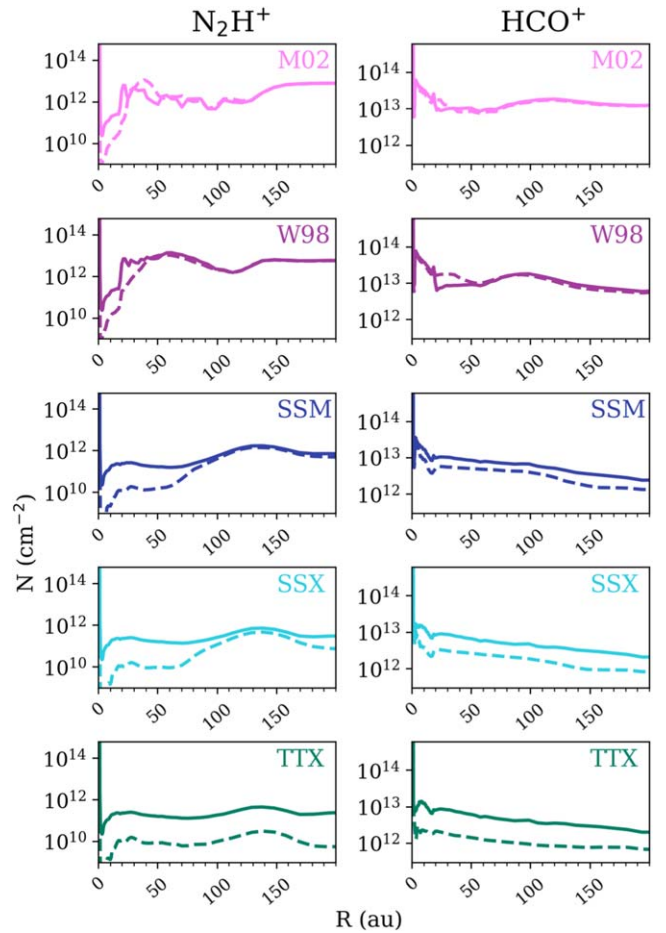


Figure 4. Vertically integrated radial column densities for N₂H⁺ (left) and HCO⁺ (right). The cosmic-ray ionization rate decreases from top to bottom, with labels corresponding to the rates listed in Table 2. Models with quiescent X-rays are shown with dashed lines while models with hardened X-rays are solid lines.

Figure 4 shows the resulting model column densities for N₂H⁺ and HCO⁺.

For N₂H⁺, increasing the CR ionization rate (ζ_{CR}) tends to increase the column density and modulates the shape of the radial column density profile. Increasing the hardness of the X-rays drives the column densities up, particularly in the inner disk. This effect becomes more pronounced throughout the disk as ζ_{CR} decreases.

For HCO⁺, we also see a general trend of increasing column density with increasing ζ_{CR} . For all of the models, we see a drop in HCO⁺ column density at the location of the dust wall at 20 au. This corresponds to increases in N₂H⁺ column density, though this is much less noticeable in the low-CR models. We expect to see this behavior because these two species are opposed in their formation pathways: N₂H⁺ thrives in the absence of gas-phase CO, while HCO⁺ requires the gas-phase CO in order to form. This relationship between the two species is most pronounced in the models with high ζ_{CR} and hard X-rays, suggesting that the formation of N₂H⁺ and HCO⁺ in the high-CR models is strongly influenced by X-ray-related chemistry in the inner disk in the presence of a dust gap. We discuss the potential role of DM Tau’s substructure in modulating ionization chemistry in more detail in Section 5.

Figure 5 shows the chemical abundances of CO, HCO⁺, and N₂H⁺ for a quiescent X-ray state and a flaring X-ray state.

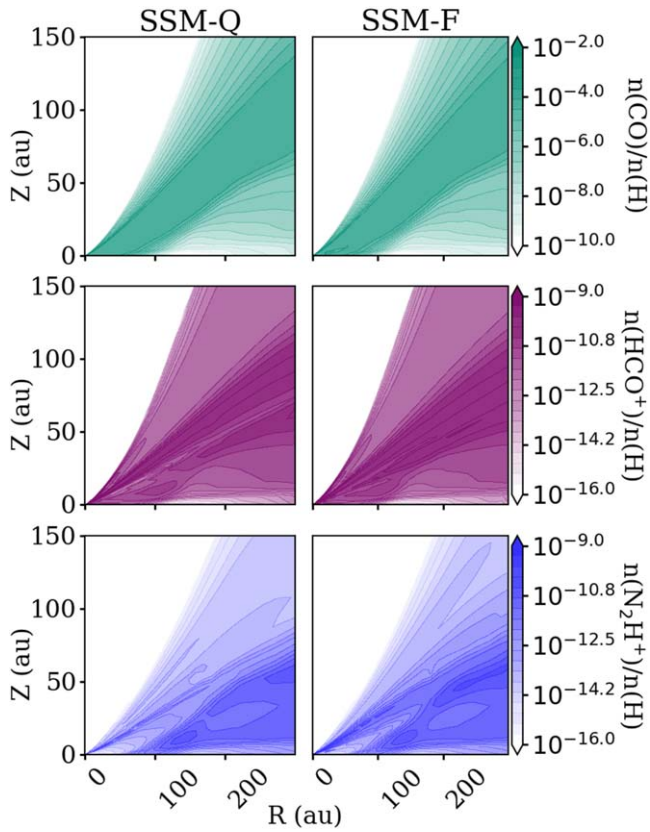


Figure 5. Comparison of SSM model abundances under quiescent and flaring X-ray conditions after 1 Myr for CO (top), HCO⁺ (middle), and N₂H⁺ (bottom).

Similar to what we see in the model column densities, both HCO⁺ and N₂H⁺ abundances appear to increase slightly in certain regions of the disk for the case of the hard X-ray spectrum, though the differences in abundance are minor. For example, there appears to be an enhancement of both N₂H⁺ and HCO⁺ at $z/r \sim 0.2$.

3.4. Synthetic Observation Comparison

The resulting disk abundances are input to the LIME non-LTE radiative transfer code (Brinch & Hogerheijde 2010) in order to calculate the emergent flux and optical depth for HCO⁺, N₂H⁺, and H¹³CO⁺. We use collisional rates from the LAMDA database (Daniel et al. 2005; Schöier et al. 2005; Denis-Alpizar et al. 2020). The LIME code includes a Doppler broadening parameter (b) that accounts for line broadening due to local turbulence. We set the Doppler velocity as a function of the local sound speed (c_s), which is temperature dependent. For our “standard turbulence” models, we use $b = 0.2c_s$. This degree of turbulence is slightly lower than the conservative turbulence estimate ($0.25c_s$) from Flaherty et al. (2020). We also run LIME models with high turbulent velocities ($b = 0.5c_s$) for comparison.

The LIME models for HCO⁺, H¹³CO⁺, and N₂H⁺ are spectrally oversampled and channel-averaged by a factor of 20 to mimic channel smearing seen in real observations. The resulting fits cubes have the same number of channels and the same channel widths as the observations listed in Table 1. All of the models assume a distance of 144.5 pc (Lindegren et al. 2018) and an inclination of 35.2° (Kudo et al. 2018).

The optical depth profiles (Figure 12 in the Appendix) show that HCO⁺ tends to be optically thick in the inner disk, as expected, while H¹³CO⁺ is optically thin throughout the disk for all models. We find that HCO⁺ appears to become more optically thin toward the inner disk (< 200 au) for low-CR and/or quiescent XR models. Both transitions of N₂H⁺ are generally optically thin throughout the disk, but become more optically thick when column densities exceed $\sim 10^{12}$ cm⁻² (this is only the case for the high-CR models). Similar to the column density profiles, we observe radial variations in the optical depth profiles corresponding to the dust gap at 20 au. Additionally, the N₂H⁺ optical depth profiles exhibit a peak between 150 and 200 au for all models, and an additional peak around 50 au that is most pronounced in the high-CR models.

We use `vis_sample` (Loomis et al. 2018) to perform visibility sampling of our LIME fits cubes. Figure 6 shows the data spectra compared to the model spectra for the standard turbulence models. By using the ALMA measurement sets from our observations as inputs, we ensure that our simulated observations have the same *uv* coverage as the real observations. We perform continuum subtraction and image the model measurement sets in CASA v.5.6.0 with the same parameters described in Section 2.

To make direct comparisons in the image plane, we produce radial profiles of the observed and modeled emission after imaging. Radial profiles are generated using the `radial_profile` function in the GoFish program (Teague 2019). We apply the same Keplerian masks used to image the observations, and we integrate emission over the same velocity ranges used to produce the moment-zero maps shown in Figure 2.

4. Results

We measure the goodness-of-fit for each model by calculating the reduced χ^2 values for the model radial profiles of HCO⁺, H¹³CO⁺, and N₂H⁺. We perform global fitting for standard and high-turbulence models (Section 4.1) as well as outer-disk fitting for standard and high-turbulence models (Section 4.2). The decision to work in the image plane was motivated by previous findings that the ionization profile of IM Lup showed a radial gradient (Seifert et al. 2021). We choose to work in the image plane so that all radii are weighted equally in our fitting routine, as opposed to the visibility plane where it is possible for brighter visibilities at long baselines to dominate the fitting results. Thus, by working in the image plane and with the radial profiles, we can more easily examine where our models are in agreement and identify ionization gradients if present. We use the radial profile reduced χ^2 values as a guide for identifying the best-fit models. While high reduced χ^2 values are expected due to the difficulty of reproducing emission across the full extent of the disk, this analysis ultimately provides a strong constraint on the best-fit model relative to the rest of the model grid.

4.1. Global Model Fitting

Observed emission reaches zero for all four lines by 500 au, so we consider radii < 500 au when calculating the global goodness-of-fit. Observed and model radial profiles for the full disk are shown in Figure 7, and the reduced χ^2 fitting results are shown in Figure 8.

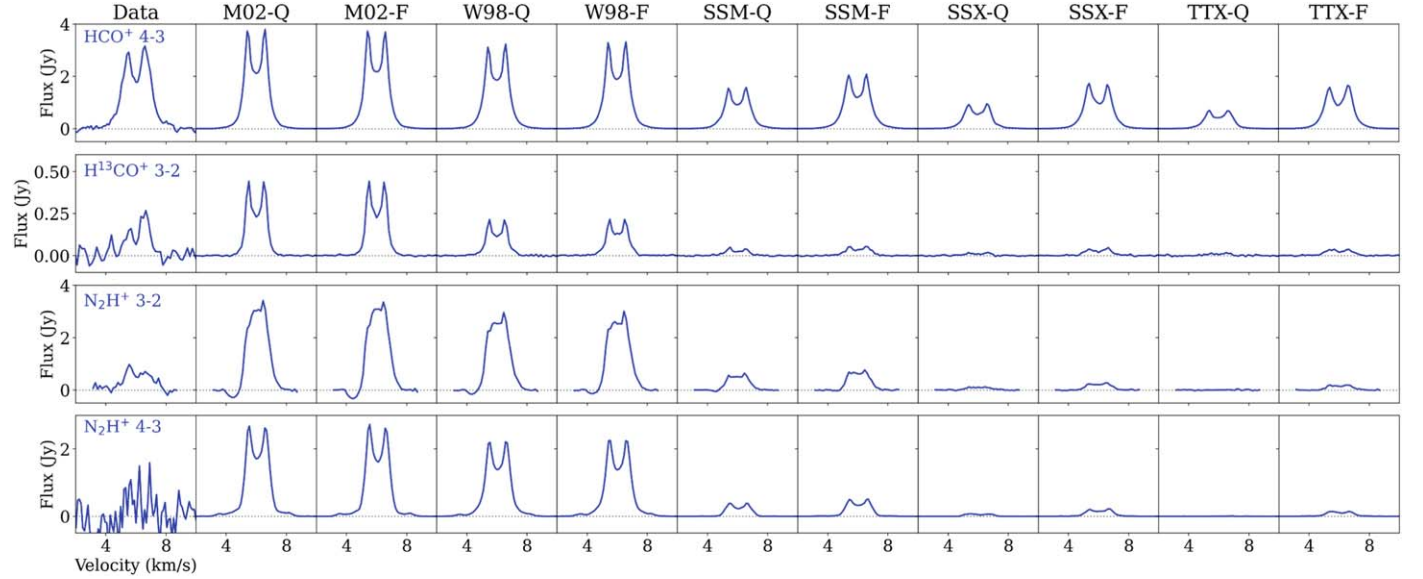


Figure 6. Observed and model spectra for the standard turbulence models produced using GoFish.

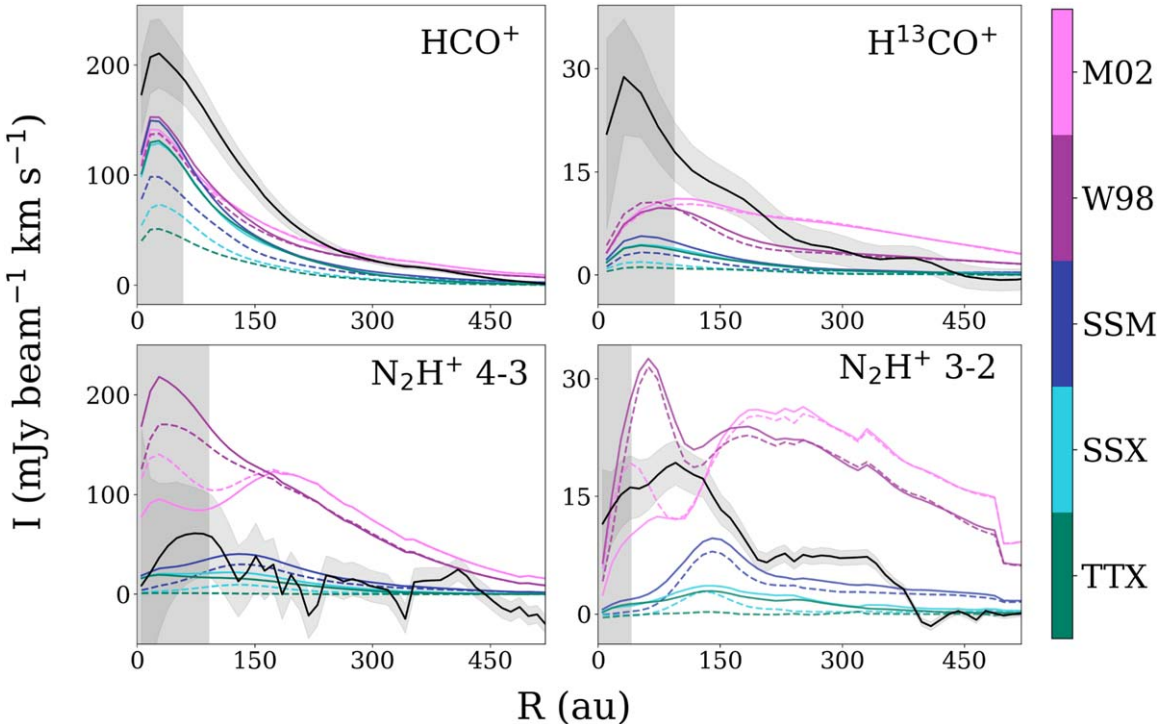


Figure 7. Observed and model radial profiles for the full disk. In each panel the solid black line is the observed emission profile and the associated light gray shading represents the uncertainties on the profile from GoFish plus the nominal 10% flux uncertainty from ALMA. The five different CR models are color-coded according to the color bar and labels on the right. For the models, dashed lines denote a quiescent XR spectrum while solid lines denote a hardened XR spectrum. The dark gray shading represents the beam of the data in au.

4.1.1. Standard Turbulence Models

We first simulate the model emission with a disk of standard turbulence ($b = 0.2c_s$). We find that the HCO^+ and H^{13}CO^+ tend to prefer a W98-F (high ionization rate) model, while in contrast the N_2H^+ lines strongly prefer a SSM-F (reduced ionization rate) model.

The observed HCO^+ and H^{13}CO^+ emission profiles each exhibit a small inner deficit and emission peaks at 30 and 40 au,

respectively. The models follow similar behavior, showing little variation in the location of the emission peak. The observed inner deficits in HCO^+ and H^{13}CO^+ emission may be related to the efficient destruction of HCO^+ by H_2O in the inner disk (Leemker et al. 2021; Notsu et al. 2021), however we expect the shapes of the emission rings seen here to be dominated by continuum opacity and excitation effects. Models with hard XR spectra have brighter peaks than their quiescent counterparts. The disparity between the hard versus quiescent

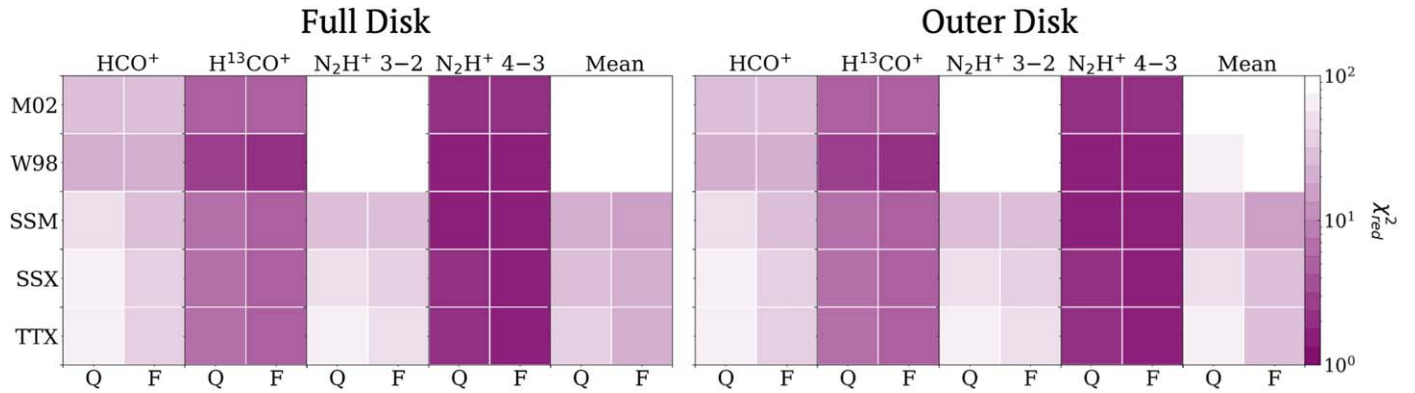


Figure 8. Reduced χ^2 fitting results for both the full disk and outer disk (>200 au). The cosmic-ray ionization rates, ζ_{CR} , are labeled on the left from high to low. On the x -axis, “Q” denotes a quiescent XR model while “F” denotes a flaring XR model. For plotting purposes, we discard extremely bad fits by cutting off reduced χ^2 values above 100, but these values still contribute to the “Mean” χ^2_{red} scores.

model emission peaks is wider for low-CR models, suggesting that hard X-ray spectra have more of an impact in low- ζ_{CR} environments ($\lesssim 10^{-18} \text{ s}^{-1}$), as expected, since X-rays can become competitive in the absence of CRs. Since the models are all underbright in the inner disk, a model that produces a bright emission peak (high ζ_{CR} and hardened XR spectrum) is preferred, and W98-F emerges as the best global fit for both HCO^+ ($\chi^2_{\text{red}} = 19.3$) and H^{13}CO^+ ($\chi^2_{\text{red}} = 2.3$).

The observed $\text{N}_2\text{H}^+ J = 3-2$ emission profile exhibits a peak at 100 au and an emission “plateau” between ~ 200 and 350 au followed by a stark drop-off. The observed profile for $\text{N}_2\text{H}^+ J = 4-3$ is very noisy due to poor atmospheric transmission at this line’s frequency, but it shows a peak around 80 au. We opt to include this line in our radial profile fitting because it demonstrates that the high-CR models are overbright, but we do not gain much insight from the emission morphology due to its being unresolved.

However, the 3–2 observations are well resolved, and we can see that our models struggle to reproduce the observed morphology. Low-CR models are underbright in the inner disk and peak further out, while high-CR models are extremely overbright in the outer disk and tend to exhibit a double-peaked structure. Since N_2H^+ is an optically thin midplane ionization tracer, this discrepancy may be indicative of CR exclusion by magnetic shearing within the disk itself (Fujii & Kimura 2022). None of the models reproduce the observed emission plateau and edge. We discuss interpretations of the modeling results for the $\text{N}_2\text{H}^+ J = 3-2$ emission morphology in depth in Section 5.2. Overall, SSM-F emerges as the best global fit for both $\text{N}_2\text{H}^+ J = 3-2$ ($\chi^2_{\text{red}} = 23.7$) and $\text{N}_2\text{H}^+ J = 4-3$ ($\chi^2_{\text{red}} = 1.48$).

As shown in the “Mean” panel of Figure 8, SSM-F is the best global fit ($\chi^2_{\text{red,mean}} = 13.8$) when we consider all four lines weighted equally. The observed emission profiles for all four lines are best fit by a model with a hard X-ray spectrum and a CR ionization rate of $1.1 \times 10^{-18} \text{ s}^{-1}$.

4.1.2. High-turbulence Models

Given the discovery of strong turbulence in this disk by Flaherty et al. (2020), we examine how including high turbulence into the broadening factor ($b = 0.5c_s$) in the radiative transfer modeling impacts our observed line emission. For lines that tend to be more optically thin, we see less of a change, while for optically thick lines more emission becomes “visible” in the image plane, and thus the velocity-integrated fluxes tend to be higher.

Increasing the turbulent velocities improves the mean χ^2_{red} scores by 4% across the full disk and 3% in the outer disk. The resulting best-fit model for each line remains unchanged aside from $\text{N}_2\text{H}^+ J = 4-3$, which changes from SSM-F to SSX-F. The χ^2_{red} score for the best-fit model for all four lines is slightly improved from 13.8 to 12.3. Thus, we consider the high-turbulence SSM-F model to be our best fit, although we do not extend this claim to suggest that this difference is enough to use these data as evidence of high turbulence alone. We discuss the nuances of this result further in Section 5.1.

4.2. Outer-disk Fitting

Examination of the radial profile morphology reveals a clear delineation between the inner and outer disk. The inner-disk emission tends to be fit best by models producing a high rate of ionization by both CRs and X-rays, while the more diffuse ionization in the outer disk is best reproduced by models with reduced rates of CR ionization. All of the models for HCO^+ and H^{13}CO^+ are underbright in the inner disk, possibly indicating that there are additional physical or chemical processes our model is not encapsulating, especially within the large gap of this disk. Moreover, our models suggest that emission from these molecules is optically thick and is not necessarily tracing the rate of ionization but rather the temperature of those regions. We perform outer-disk fitting in order to isolate the regions in which these molecules may offer constraints on the rate of ionization in the outer disk (Figure 9).

We consider the outer disk to be radii >200 au, as this is the radius at which HCO^+ and H^{13}CO^+ are no longer universally underbright. Additionally, 200 au is the radius at which $\text{N}_2\text{H}^+ J = 3-2$ emission “swaps” from preferring the high-CR models to low-CR models. In terms of disk structure, the dust disk is smooth beyond the gap at 111 au (Hashimoto et al. 2021) so we do not expect any complexities due to substructure to have an effect exterior to 111 au. Thus, 200 au is a reasonable choice for representing the shift in chemistry and physics from inner disk to outer disk.

There are some notable changes in our χ^2_{red} fitting results when we consider only the outer disk (Figure 8). HCO^+ shifts to favor an even higher CR rate (M02), while H^{13}CO^+ sees an increase in agreement for the lower-CR models and a relative decrease in agreement for M02. Extremely reduced CR rates (SSX and TTX) are further ruled out for $\text{N}_2\text{H}^+ J = 3-2$ while extremely high CR rates are further ruled out for $\text{N}_2\text{H}^+ J = 4-3$. The best-fit model for all four lines is still SSM-F, for

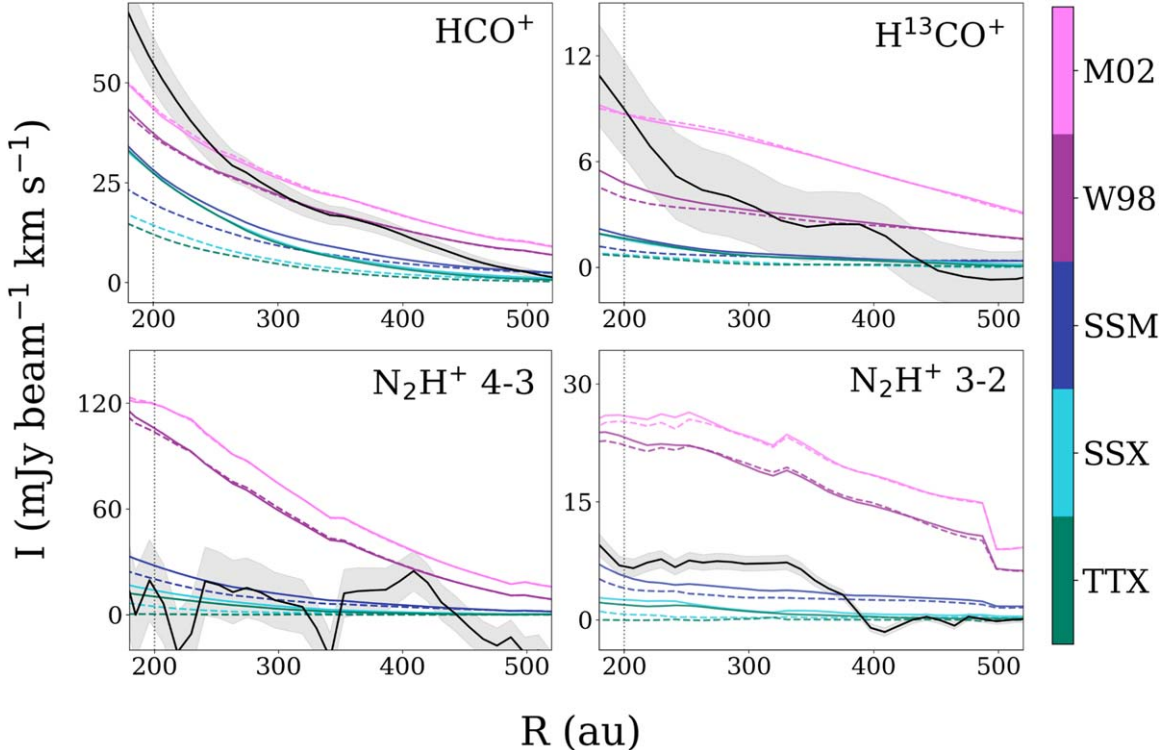


Figure 9. Observed and model radial profiles for the outer disk ($R > 200$ au). In each panel the solid black line is the observed emission profile and the associated light gray shading represents the uncertainties on the profile from GoFish plus the nominal 10% flux uncertainty from ALMA. The dashed vertical line marks 200 au, which we consider to be the transition radius from inner to outer disk. The five different CR models are color-coded according to the color bar and labels on the right. For the models, dashed lines denote a quiescent XR spectrum while solid lines denote a hardened XR spectrum.

both the standard ($\chi^2_{\text{red}} = 17.3$) and high-turbulence ($\chi^2_{\text{red}} = 12.8$) models.

5. Discussion

5.1. The Ionization Environment of DM Tau

Our modeling of HCO^+ , H^{13}CO^+ , and N_2H^+ suggests that a high rate of ionization is required to reproduce bright emission of molecular ions in the inner disk, while a lower rate of ionization by CRs is required to fit the outer disk where the observed emission from all four lines is much more diffuse. This result is consistent with a strongly ionized inner disk followed by a steep ionization gradient and a low ionization rate in the outer disk. Previous studies that suggest the presence of CR gradients in TW Hya and IM Lup (Cleeves et al. 2015; Seifert et al. 2021) found the opposite trend of ζ_{CR} suppression in the inner disk and, in the case of IM Lup, an increase in ζ_{CR} toward the outer disk. TW Hya is close to DM Tau in age ($\sim 3\text{--}10$ Myr; Vacca & Sandell 2011) and disk mass ($0.05 M_{\odot}$; Bergin et al. 2013), while IM Lup is both younger (1 Myr; Mawet et al. 2012) and more massive ($\sim 0.1 M_{\odot}$; Pinte et al. 2008). While both TW Hya and IM Lup exhibit substructure in their continuum emission (Huang et al. 2018), neither of these disks has a large inner cavity like DM Tau’s 20 au gap.

The suppression of CR ionization in TW Hya and IM Lup can be explained by the presence of a disk wind blocking external ionizing radiation from reaching the inner disk. It is less straightforward to explain a CR gradient in the case of DM Tau, as we would not expect there to be a “barrier” blocking incident external CRs from reaching the outer disk while allowing them to ionize the inner disk. Rather than a reduced rate of ionization in the inner disk like IM Lup or TW Hya, DM

Tau appears to have some kind of ionization enhancement localized to the inner ~ 150 au.

In the outer disk, if one compares the observed H^{13}CO^+ and HCO^+ to the models without considering the N_2H^+ , the model with an ISM-like CR rate ($\zeta_{\text{CR}} \sim 10^{-17} \text{ s}^{-1}$) appears to fit reasonably well; however, changes to the CO depletion profile impact the fit to a similar degree (Section 5.3), and also within the uncertainty of the more optically thin H^{13}CO^+ outer-disk profile. Given that H^{13}CO^+ and N_2H^+ trace different vertical regions of the outer disk, if this tension holds with deeper observations, perhaps the data are pointing to a steeper vertical gradient than what is captured in the present models. One possible theory is CR exclusion within the disk itself by magnetic shearing (Fujii & Kimura 2022), where CRs are significantly detoured on their way to the disk midplane prior to reaching the N_2H^+ layer. The sensitivity of the data is not sufficient to definitively say, but it provides an interesting avenue for future follow-up.

Both DM Tau and IM Lup exhibit evidence of turbulence in the upper layers of the outer regions of their disks, while TW Hya does not (Flaherty et al. 2020, 2024). While DM Tau and IM Lup each have unique ionization structures, both disks have higher rates of CR ionization ($\gtrsim 10^{-18} \text{ s}^{-1}$) than TW Hya ($\lesssim 10^{-19} \text{ s}^{-1}$). Our results alone do not suggest definitively that DM Tau’s turbulence is MRI driven. However, we do find that the inner disk is particularly well ionized compared to the outer disk. The relatively high degree of ionization in the inner disk may be related to the large 20 au dust gap or another mechanism not captured by our modeling efforts. While we cannot identify the exact mechanism in this work, it is clear that ionizing radiation from the central star plays an important role in the inner disk and could play a role in driving DM Tau’s previously discovered turbulence. Robust constraints on disk

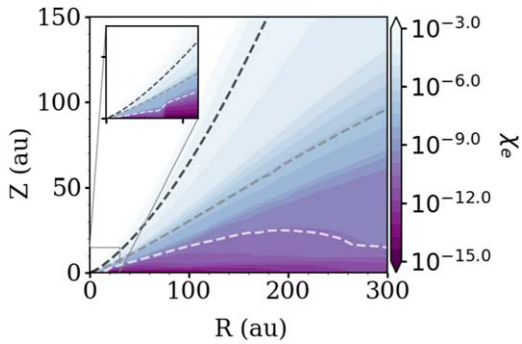


Figure 10. Two-dimensional ionization fraction (shown as the fraction of electrons, χ_e) for our best-fit model, SSM-F. The black, gray, and white contours represent ionization fractions of 1×10^{-4} , 1×10^{-7} , and 1×10^{-10} , respectively.

turbulence and ionization in larger samples will be critical for understanding the role of ionization in facilitating the redistribution of disk material via the MRI.

Our global best-fit model, SSM-F, is an intermediate- ζ_{CR} model with a flaring X-ray state. This model comes closest to reproducing the bright emission from molecular ions in the inner disk without overproducing emission from molecular ions in the outer disk. Figure 10 shows the 2D ionization fraction for the SSM-F model. Our best-fit model suggests that the ionization fraction in DM Tau varies from $\chi_e > 1 \times 10^{-4}$ at the surface to $\chi_e < 1 \times 10^{-10}$ in the midplane, in agreement with previous estimates of DM Tau’s ionization fraction (Öberg et al. 2011; Teague et al. 2015). The inner-disk emission from molecular ions in DM Tau is difficult to reproduce using our model under “normal” assumptions. Even our highest- ζ_{CR} models with hardened X-ray spectra are unable to reproduce the bright inner-disk emission from H^{13}CO^+ and N_2H^+ —both optically thin tracers. All of this suggests that our models fail to capture some aspects of the chemistry and physics that may be enhancing ionization in DM Tau’s inner disk.

In our models, we vary CR ionization and test the effects of X-ray variability by including both quiescent and hardened X-ray spectra. In reality, there may be more complex physics at play. It is possible that the deficit of material within 20 au allows the disk beyond 20 au to be more readily ionized by X-rays, since the attenuation along lines of sight to the star is less than for a full disk. Additionally, ionization by X-rays impacting the inner disk could be nonuniform due to shadowing from an asymmetric and/or misaligned inner dust disk. High-resolution dust continuum images from Hashimoto et al. (2021) show two asymmetries in the 20 au dust ring, and suggest that the inner ring at 3 au could be misaligned from the outer ring at 20 au, though their visibility analyses find that the rings’ PA and inclination values agree within 3σ .

Another possible cause of an elevated inner-disk ionization state could be additional ionization from stellar energetic particles (SPs). Modeling by Rab et al. (2017) suggests that while SPs cannot penetrate the disk midplane, they can dominate ionization in the warm molecular layer for regions close to the star. As a result of additional ionization by SPs, HCO^+ and N_2H^+ column densities may be elevated by a factor of $\sim 3\text{--}10$ in the inner disk (≤ 200 au), especially for models with low CR ionization rates. The SP ionization rate for the active T Tauri star model in Rab et al. (2017) is $\zeta_{\text{SP}} \sim 10^{-13}\text{--}10^{-12} \text{ s}^{-1}$ at a vertical column of 10^{21} cm^{-2} . This rate is significantly higher than both the quiescent and “flaring” XR

ionization rates in our models ($\zeta_{\text{XR}} \sim 10^{-15}\text{--}10^{-14} \text{ s}^{-1}$) for the same gas column at 10 au. This suggests that SPs could be a competitive source of ionization in DM Tau’s inner disk, possibly explaining the elevated emission in HCO^+ , H^{13}CO^+ , and N_2H^+ that we observe. Additionally, Cabedo et al. (2023) find enhanced ionization at small radii that may be explained by CR acceleration close to the B335 protostar. Both of these results suggest that SPs and CR acceleration close to the central star could play a role in boosting inner-disk ionization.

5.2. N_2H^+ Radial Structure

Since N_2H^+ forms efficiently in the absence of gas-phase CO, observations of this molecule have been used to probe the CO snowline (Qi et al. 2013). The emission peak of $\text{N}_2\text{H}^+ J = 3\text{--}2$ has previously been interpreted as a direct tracer of CO freeze-out in DM Tau (Qi et al. 2019), however our models struggle to reproduce the location of the peak $\text{N}_2\text{H}^+ J = 3\text{--}2$ emission at 100 au (Figure 7, lower-right panel). Low-CR models (SSM, SSX, and TTX) produce peak emission closer to 135 au. High-CR models (M02 and W98) produce two “peaks,” at ~ 55 au and $\sim 170\text{--}180$ au. Model N_2H^+ emission is enhanced by an X-ray flare if present, except for the inner-disk emission for the M02 model, which follows the opposite behavior. No models reproduce the emission plateau and subsequent drop-off between 300 and 400 au. While the SSM-F model emerges as the best global fit for this line ($\chi^2 = 23.7$), it does not reproduce the observed emission peak. An examination of the radial emission morphology for this line offers several other possible interpretations.

If we follow the interpretation of the N_2H^+ emission peak as a direct tracer of the CO snowline in DM Tau, then it could be the case that our models have too much gas-phase CO in the inner disk, leading to the underproduction of N_2H^+ at 100 au. Zhang et al. (2019) found that the level of CO depletion in DM Tau ranges from a factor of ~ 10 in the inner disk to a factor of ~ 1 in the outer disk. We use an “average” (factor of 5) in our models, but it is possible that a more detailed model with radial CO depletion is necessary to reproduce the N_2H^+ emission morphology, particularly in the inner disk where CO is most depleted.

Our average-depleted model yields a C^{18}O integrated flux of 4.9 Jy km s^{-1} , which agrees to within a factor of 2 of the 3.0 Jy km s^{-1} C^{18}O flux reported by Zhang et al. (2019). The difference in flux is likely due to the fact that our gas model has a smoothly continuous inner disk. Our overprediction of C^{18}O in the inner disk is consistent with a more radiation-permeable inner disk, which could also increase the HCO^+ abundance in this inner region. Detailed modeling of the impact of the inner-disk gas structure is left to future work as it requires higher-resolution molecular-ion data of the inner disk.

Since N_2H^+ is also a key constraint on ionization in the outer disk, and thus motivates our findings of a reduced ζ_{CR} , we test the robustness of our $\text{N}_2\text{H}^+ J = 3\text{--}2$ fits with varying CO depletion. We compared the radial profile results from our “average” (factor of 5) depletion model to those from models with no CO depletion and a factor of 10 CO depletion. The resulting $\text{N}_2\text{H}^+ J = 3\text{--}2$ radial profiles are relatively insensitive to the level of CO depletion (varying by a factor of < 2 in flux), and the effect of CRs dominates the effect of CO depletion in the outer disk. Thus, even if we leave CO undepleted, a reduced rate of ionization is required to fit the observations.

Another possibility discussed in Section 5.1 is the presence of a radial gradient in CRs. It is clear from the models that the

N_2H^+ distribution observed in the disk is very sensitive to the assumptions about CR and X-ray fluxes. However, if CRs are responsible, the outer disk provides strong constraints on the absence of CR ionization. Thus, some other mechanism causing additional ionization close to the star or attenuation of CRs in the outer disk is required that is not taken into account in our models.

Finally, another mechanism that could reproduce the N_2H^+ peak is a change in the model's midplane temperature. Our temperature model was derived from observations of CO, which do not explicitly probe the midplane. However, using the RADEX radiative transfer code (van der Tak et al. 2007), the ratio of observed fluxes between the $J = 4-3$ and $J = 3-2$ transitions at 100 au suggests a temperature of 25 K. This agrees with our model temperatures at 100 au, which range between 20 and 30 K from midplane to surface. Qi et al. (2019) are able to reproduce the N_2H^+ $J = 3-2$ radial profile by including a vertically isothermal region above the midplane (VIRaM layer) in their temperature model. While our CO-derived temperature structure appears to produce reasonable midplane temperatures based on the N_2H^+ line ratio, future work with stronger midplane temperature constraints and detailed features such as a VIRaM layer could improve the fit for the N_2H^+ emission peak and offer additional insight into midplane ionization.

Ultimately, the emission morphology of N_2H^+ is dependent on a combination of effects from ionization, temperature, and gas-phase CO abundance. These parameters/processes are degenerate with one another, and additional modeling efforts are necessary to disentangle their effects. While we do not explore this degeneracy fully in this work, such efforts will help to determine the usefulness of N_2H^+ as a direct observational tracer of the CO snowline as well as its usefulness for constraining midplane ionization in a larger sample.

5.3. Sensitivity to CO Depletion Profile

We tested the sensitivity of our models to the CO depletion profile by running an additional model grid with no CO depletion (initial CO abundance = 1.3×10^{-4}). As discussed above in Section 5.2, one possible explanation for the lack of inner-disk emission from N_2H^+ in our models was an overabundance of gas-phase CO (a factor of 5 depletion compared to the factor of 10 depletion inferred by Zhang et al. 2019). However, decreasing the amount of CO in the inner disk also leads to a decrease in HCO^+ and H^{13}CO^+ , which contradicts what we observe. As shown in Figure 11, increasing the initial CO abundance for the model grid results in brighter H^{13}CO^+ and dimmer N_2H^+ in the inner disk. This aligns with our expectations, as H^{13}CO^+ forms readily in the presence of CO while N_2H^+ is destroyed. Both species are sensitive to the degree of CO depletion, but in opposite ways.

Since brighter inner-disk fluxes are required to fit the observed emission for both species, the CO depletion profile itself cannot account for the “boost” in emission in the inner disk. In the outer disk, where we expect there to be little to no CO depletion (Zhang et al. 2018), high-CR models can be ruled out for both H^{13}CO^+ and N_2H^+ , further motivating the presence of CR shielding across the full disk extent. In reality, DM Tau likely exhibits a complex CO depletion profile (higher depletion possibly increasing N_2H^+ production in the inner disk) as well as additional physical processes leading to an increase in ionizing radiation, which would account for the bright inner-disk emission from both species.

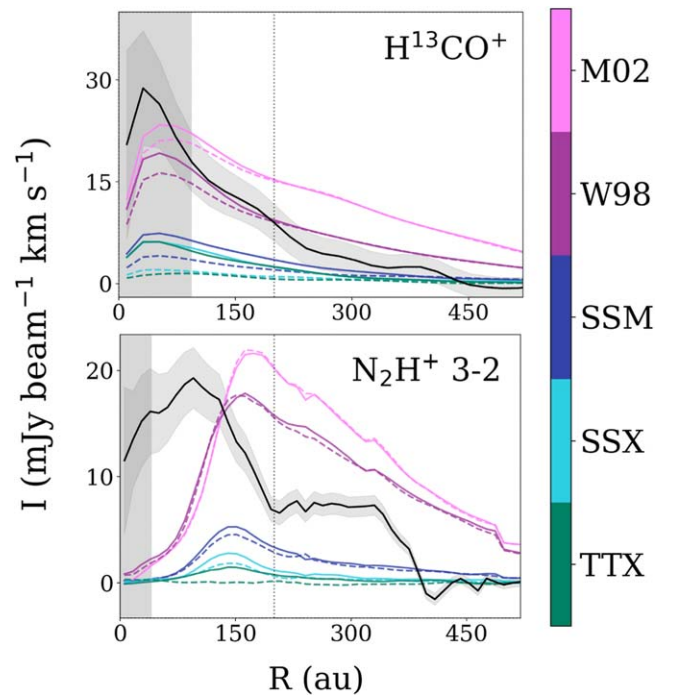


Figure 11. Observed and model radial profiles of H^{13}CO^+ and N_2H^+ for the models with no CO depletion. The five different CR models are color-coded according to the color bar and labels on the right while the observed profiles are plotted in solid black. Dashed lines denote models with a quiescent XR spectrum while solid lines denote a hardened XR spectrum.

5.4. Uses of Different Ionization Tracers

By forward modeling the DM Tau disk in detail, we are not only able to gain valuable insights to the ionization environment of this system but also examine the usefulness of each of the ionization tracers included in this work. $\text{HCO}^+ J = 4-3$ is considered to be an optically thick tracer, while $\text{H}^{13}\text{CO}^+ J = 3-2$ is expected to be optically thin. In DM Tau, we see bright HCO^+ emission coming from the high-velocity wings, suggesting that there is no significant depletion of gas in the inner disk despite the large 20 au dust cavity. In more compact sources it is possible that HCO^+ could be optically thin in the inner disk. Thus, this tracer could be very useful for constraining inner-disk conditions for compact sources. In bright sources, it is clear that H^{13}CO^+ is a necessary complementary line to observe in addition to optically thick HCO^+ .

Models and observations of HCO^+ suggest that its abundance in the disk surface can be altered by rapid X-ray changes from the central star, such as X-ray flares (Waggner & Cleeves 2022; Waggner et al. 2023). All of our DM Tau models with a hardened “flaring” XR spectrum have brighter peaks than their quiescent counterparts, though the disparity is wider for low-CR models. Our models suggest that in the presence of high- ζ_{CR} conditions (M02, W98), the effect of an X-ray flare on the emission of optically thick HCO^+ is subtle, only changing the peak profile intensity (ΔI_{peak}) by an average of $5 \text{ mJy beam}^{-1} \text{ km s}^{-1}$. On the other hand, an X-ray flare under low- ζ_{CR} conditions (SSM, SSX, TTX) will have a more noticeable effect on the observed HCO^+ emission, with $\Delta I_{\text{peak}} = 50-80 \text{ mJy beam}^{-1} \text{ km s}^{-1}$. Thus, if one wants to observe the effects of X-ray flares using HCO^+ , sources with low ζ_{CR} may be favorable targets.

As discussed in Section 5.2, there are several interpretations of our modeling results for N_2H^+ , and it is not fully clear

whether or not N_2H^+ is a direct tracer of the CO snowline in DM Tau. Larger samples with sensitive and resolved observations of additional N_2H^+ transitions and/or other optically thin ionization tracers which form in the presence of gas-phase CO (e.g., H^{13}CO^+ and DCO^+) will help to guide modeling efforts to clarify the role of N_2H^+ as a direct tracer of CO freeze-out. Overall, N_2H^+ is an effective cold ionization tracer that is sensitive to both CRs and X-rays. N_2H^+ may be particularly enhanced in disks with substructure that allows for the penetration of X-rays deeper into the disk midplane.

It is important to use multiple tracers that probe different disk emitting heights to interpret the ionization environments of protoplanetary disks. DM Tau exhibits evidence of both radial and vertical ionization gradients. In our fitting of the radial profiles, a boost in inner-disk ionization is required for all three molecular ions even for some of the highest-CR models. When we consider the different emitting heights of our optically thin tracers H^{13}CO^+ and N_2H^+ , their emission profiles suggest a vertical gradient in CR ionization that may not be explained by attenuation alone. Overall, the small sample of disks with well-characterized ionization environments—DM Tau, TW Hya, and IM Lup—exhibit a variety of ionization structures which appear to be impacted by different shielding mechanisms at different disk locations. An exploration of both radial and vertical ionization gradients is required in order to differentiate between the many factors governing disks' complex ionization environments. Thus, studies of disk ionization should include resolved observations of at least two optically thin tracers tracing distinct disk emitting heights.

6. Conclusions

We present new observations of $\text{HCO}^+ J = 4-3$, $\text{H}^{13}\text{CO}^+ J = 3-2$, and $\text{N}_2\text{H}^+ J = 4-3$ in the DM Tau protoplanetary disk. Using these observations, along with archival observations of $\text{N}_2\text{H}^+ J = 3-2$, we aim to forward model DM Tau's ionization environment. Our main findings are as follows:

1. When considering all three molecular ions, DM Tau's ionization state is best fit by a model with a CR ionization rate an order of magnitude lower than that of the ISM ($\zeta_{\text{CR}} = 1.1 \times 10^{-18} \text{ s}^{-1}$) and a hardened X-ray spectrum, postprocessed with high turbulent velocities ($b = 0.5c_s$). The improvement with high turbulent velocity is not significant, but leads to slightly better fits. The ionization fraction in our best-fit model varies from $\chi_e > 1 \times 10^{-4}$ at the surface to $\chi_e < 1 \times 10^{-10}$ in the midplane.
2. DM Tau exhibits a steep drop in ionization from the inner disk to the outer disk that our models struggle to reproduce with one ionization rate ζ_{CR} . We speculate that disk has some shielding mechanism reducing the incident CR rate across the full 500 au extent, but that there are either (i) additional physical effects not modeled, like SPs, or (ii) the presence of substructure making the inner disk more permeable to CRs. Both of these scenarios deserve dedicated modeling efforts.
3. Our observations appear to trace a flaring state of DM Tau ($\text{HR} = 0.3$). In our fitting of individual lines, all four are best fit by models with the hardened X-ray spectrum. Additional observations of HCO^+ , H^{13}CO^+ , and N_2H^+ in DM Tau at different epochs could reveal evidence of X-ray variability.

This study provides new constraints on DM Tau's ionization environment through detailed 2D forward modeling. Our methods allow us to examine the roles of different sources of ionization, leading to a better understanding of the physical and chemical conditions governing disk evolution and planet formation. This work highlights the need for multiline studies, which will allow us to probe different vertical layers of the disk. By combining molecules that trace different layers and by examining the spatially resolved radial profiles, we are able to rule out a high CR ionization rate across the full radial and vertical disk extent and identify a possible enhancement occurring within the inner disk of DM Tau. In general, constraining ionization in protoplanetary disks remains challenging because (i) ionization is provided by a diverse set of sources, (ii) the efficacy of those sources varies throughout the disk, and (iii) the sources vary from disk to disk. High-resolution, multiline studies of ionization tracers in large samples will be critical for disentangling the complexity of disk ionization and its sources.

Acknowledgments

We thank the anonymous referee for their insightful comments that improved the quality of this manuscript. D.E.L. thanks Z. Y. Li and R. A. Loomis for helpful discussions about the results presented in this paper. This paper makes use of the following ALMA data: ADS/JAO.ALMA #2019.1.00379.S and ADS/JAO.ALMA #2015.1.00678.S. ALMA is a partnership of ESO (representing its member states), NSF (USA), and NINS (Japan), together with NRC (Canada), MOST and ASIAA (Taiwan), and KASI (Republic of Korea), in cooperation with the Republic of Chile. The Joint ALMA Observatory is operated by ESO, AUI/NRAO, and NAOJ. The National Radio Astronomy Observatory is a facility of the National Science Foundation operated under cooperative agreement by Associated Universities, Inc. We are grateful to the Atacameño (Likan Antai) Elders—the first astronomers of Atacama—whose wisdom and knowledge we continue to learn and benefit from as ALMA users. D.E.L. and L. I.C. acknowledge support from NASA ATP grant No. 80NSSC20K0529. D.E.L. also acknowledges support from the Virginia Space Grant Consortium. L.I.C. also acknowledges support from NSF grant No. AST-2205698, the David and Lucille Packard Foundation, and the Research Corporation for Scientific Advancement Cottrell Scholar Award. V.V.G. gratefully acknowledges support from FONDECYT Regular 1221352 and ANID CATA-BASAL project FB210003. The modeling conducted in this paper was carried out on the University of Virginia's Rivanna High Performance Computing Cluster.

Facility: ALMA.

Software: CASA (McMullin et al. 2007), LIME (Brinch & Hogerheijde 2010), vis_sample (Loomis et al. 2018), bettermoments (Teague & Foreman-Mackey 2018), GoFish (Teague 2019), keplerian_mask (Teague 2020).

Appendix

Azimuthally Averaged Optical Depth Profiles

Figure 12 shows the azimuthally averaged optical depth profiles of $\text{HCO}^+ J = 4-3$, $\text{H}^{13}\text{CO}^+ J = 3-2$, $\text{N}_2\text{H}^+ J = 4-3$, and $\text{N}_2\text{H}^+ J = 3-2$ for the grid of models described in Section 3.

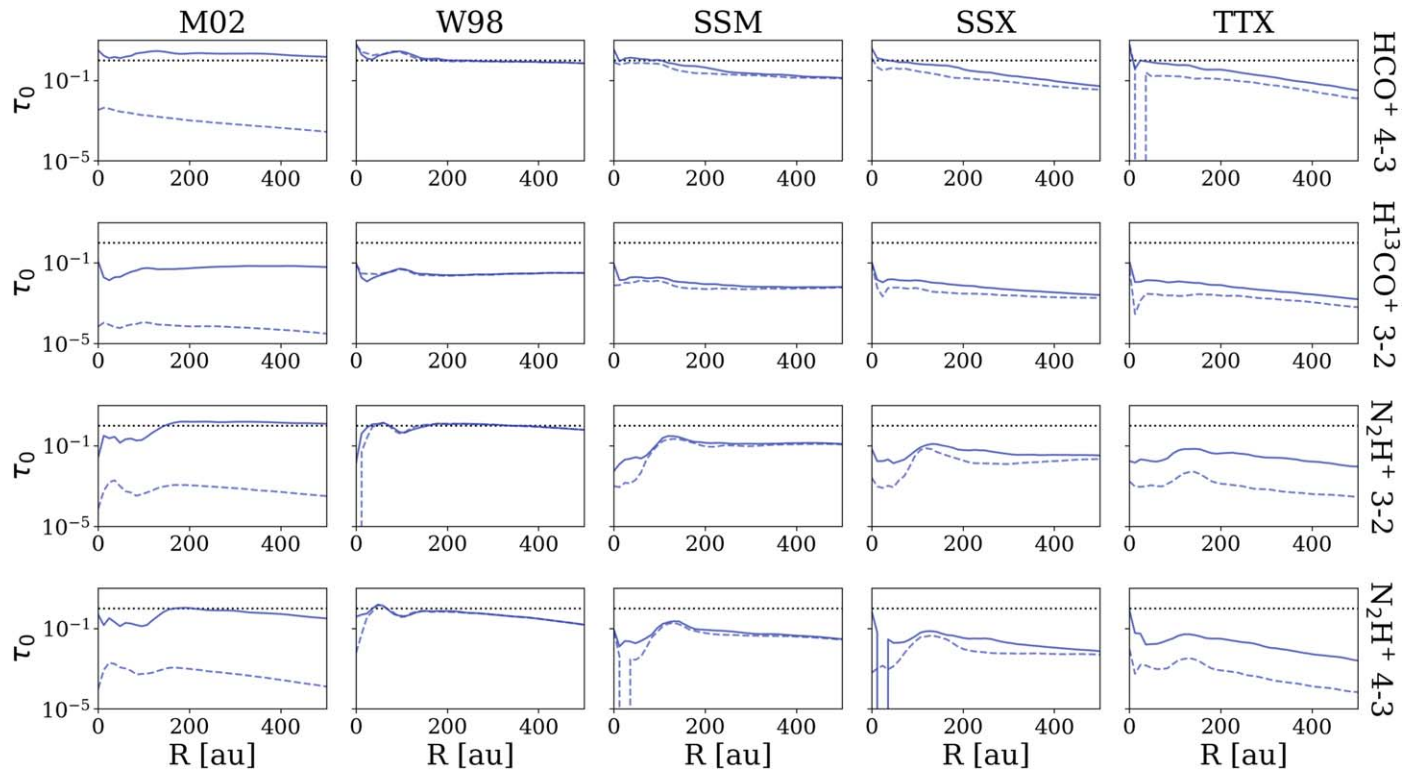


Figure 12. Model optical depth profiles produced with `LIME`. The dotted black line shows the $\tau = 1$ surface. The column labels (top) denote the five different CR models and the row labels (right) denote the four different molecular lines. Dashed lines represent models with a quiescent XR spectrum and solid lines represent models with a hardened XR spectrum.

ORCID iDs

Deryl E. Long [ID](https://orcid.org/0000-0003-3840-7490) <https://orcid.org/0000-0003-3840-7490>
 L. Ilsedore Cleeves [ID](https://orcid.org/0000-0003-2076-8001) <https://orcid.org/0000-0003-2076-8001>
 Fred C. Adams [ID](https://orcid.org/0000-0002-8167-1767) <https://orcid.org/0000-0002-8167-1767>
 Sean Andrews [ID](https://orcid.org/0000-0003-2253-2270) <https://orcid.org/0000-0003-2253-2270>
 Edwin A. Bergin [ID](https://orcid.org/0000-0003-4179-6394) <https://orcid.org/0000-0003-4179-6394>
 Viviana V. Guzmán [ID](https://orcid.org/0000-0003-4784-3040) <https://orcid.org/0000-0003-4784-3040>
 Jane Huang [ID](https://orcid.org/0000-0001-6947-6072) <https://orcid.org/0000-0001-6947-6072>
 A. Meredith Hughes [ID](https://orcid.org/0000-0002-4803-6200) <https://orcid.org/0000-0002-4803-6200>
 Chunhua Qi [ID](https://orcid.org/0000-0001-8642-1786) <https://orcid.org/0000-0001-8642-1786>
 Kamber Schwarz [ID](https://orcid.org/0000-0002-6429-9457) <https://orcid.org/0000-0002-6429-9457>
 Jacob B. Simon [ID](https://orcid.org/0000-0002-3771-8054) <https://orcid.org/0000-0002-3771-8054>
 David Wilner [ID](https://orcid.org/0000-0003-1526-7587) <https://orcid.org/0000-0003-1526-7587>

References

Adams, F. C. 2010, *ARA&A*, **48**, 47
 Aikawa, Y., Cataldi, G., Yamato, Y., et al. 2021, *ApJS*, **257**, 13
 Anderson, D. E., Blake, G. A., Cleeves, L. I., et al. 2021, *ApJ*, **909**, 55
 Andrews, S. M., Wilner, D. J., Espaillat, C., et al. 2011, *ApJ*, **732**, 42
 Bai, X.-N. 2015, *ApJ*, **798**, 84
 Balbus, S. A., & Hawley, J. F. 1991, *ApJ*, **376**, 214
 Bergin, E. A., Aikawa, Y., Blake, G. A., & van Dishoeck, E. F. 2007, in *Protostars and Planets*, ed. B. Reipurth, D. Jewitt, & K. Keil (Tucson, AZ: Univ. Arizona Press), 751
 Bergin, E. A., Cleeves, L. I., Crockett, N. R., Favre, C., & Neill, J. L. 2013, in *ASP Conf. Ser.* 476, *New Trends in Radio Astronomy in the ALMA Era: The XXX Anniversary of Nobeyama Radio Observatory*, ed. R. Kawabe, N. Kuno, & S. Yamamoto (San Francisco, CA: ASP), 185
 Bergner, J. B., Öberg, K. I., Bergin, E. A., et al. 2020, *ApJ*, **898**, 97
 Bethell, T. J., & Bergin, E. A. 2011, *ApJ*, **739**, 78
 Blandford, R. D., & Payne, D. G. 1982, *MNRAS*, **199**, 883
 Blum, J. 2018, *SSRv*, **214**, 52
 Brinch, C., & Hogerheijde, M. R. 2010, *A&A*, **523**, A25
 Cabedo, V., Maury, A., Girart, J. M., et al. 2023, *A&A*, **669**, A90
 Chen, K., & Lin, M.-K. 2020, *ApJ*, **891**, 132
 Clarke, C. J. 2007, *MNRAS*, **376**, 1350
 Cleeves, L. I., Adams, F. C., & Bergin, E. A. 2013, *ApJ*, **772**, 5
 Cleeves, L. I., Bergin, E. A., Alexander, C. M. O., et al. 2014, *Sci*, **345**, 1590
 Cleeves, L. I., Bergin, E. A., Qi, C., Adams, F. C., & Öberg, K. I. 2015, *ApJ*, **799**, 204
 Cleeves, L. I., Öberg, K. I., Wilner, D. J., et al. 2016, *ApJ*, **832**, 110
 Damiani, F., Micela, G., Sciortino, S., & Harnden, F. R., Jr. 1995, *ApJ*, **446**, 331
 Daniel, F., Dubernet, M.-L., Meuwly, M., Cernicharo, J., & Pagani, L. 2005, *MNRAS*, **363**, 1083
 Dartois, E., Dutrey, A., & Guilloteau, S. 2003, *A&A*, **399**, 773
 Denis-Alpizar, O., Stoecklin, T., Dutrey, A., & Guilloteau, S. 2020, *MNRAS*, **497**, 4276
 Eistrup, C., Walsh, C., & van Dishoeck, E. F. 2018, *AA*, **613**, A14
 Flaherty, K., Hughes, A. M., Simon, J. B., et al. 2020, *ApJ*, **895**, 109
 Flaherty, K., Hughes, A. M., Simon, J. B., et al. 2024, Evidence for non-zero turbulence in the protoplanetary disc around IM Lup, *MNRAS*, **532**, 363
 Fleming, T., & Stone, J. M. 2003, *ApJ*, **585**, 908
 Fogel, J. K. J., Bethell, T. J., Bergin, E. A., Calvet, N., & Semenov, D. 2011, *ApJ*, **726**, 29
 Foreman-Mackey, D., Hogg, D. W., Lang, D., & Goodman, J. 2013, *PASP*, **125**, 306
 Fujii, Y. I., & Kimura, S. S. 2022, *ApJL*, **937**, L37
 Gole, D., Simon, J. B., Lubow, S. H., & Armitage, P. J. 2016, *ApJ*, **826**, 18
 Gole, D. A., Simon, J. B., Li, R., Youdin, A. N., & Armitage, P. J. 2020, *ApJ*, **904**, 132
 Hashimoto, J., Muto, T., Dong, R., et al. 2021, *ApJ*, **911**, 5
 Herbst, E., & Klempner, W. 1973, *ApJ*, **185**, 505
 Huang, J., Andrews, S. M., Dullemond, C. P., et al. 2018, *ApJ*, **869**, L42
 Igata, J., & Glassgold, A. E. 1999, *ApJ*, **518**, 848
 Johansen, A., Oishi, J. S., Mac Low, M.-M., et al. 2007, *Nature*, **448**, 1022
 Klahr, H., & Hubbard, A. 2014, *ApJ*, **788**, 21
 Kudo, T., Hashimoto, J., Muto, T., et al. 2018, *ApJ*, **868**, L5
 Langer, W. D., & Penzias, A. A. 1993, *ApJ*, **408**, 539
 Leemker, M., van't Hoff, M. R., Trapman, L., et al. 2021, *A&A*, **646**, A3
 Lim, J., Simon, J. B., Li, R., et al. 2024, *ApJ*, **969**, 130

Lindegren, L., Hernández, J., Bombrun, A., et al. 2018, *A&A*, **616**, A2

Loomis, R. A., Öberg, K. I., Andrews, S. M., et al. 2018, *AJ*, **155**, 182

Marcus, P. S., Pei, S., Jiang, C.-H., et al. 2015, *ApJ*, **808**, 87

Mathis, J. S., Rumpl, W., & Nordsieck, K. H. 1977, *ApJ*, **217**, 425

Mawet, D., Absil, O., Montagnier, G., et al. 2012, *A&A*, **544**, A131

McMullin, J. P., Waters, B., Schiebel, D., Young, W., & Golap, K. 2007, in *ASP Conf. Ser.* 376, *Astronomical Data Analysis Software and Systems XVI*, ed. R. A. Shaw, F. Hill, & D. J. Bell (San Francisco, CA: ASP), **127**

Melon Fuksman, J. D., Flock, M., & Klahr, H. 2024, *A&A*, **682**, A139

Miotello, A., Kamp, I., Birnstiel, T., Cleeves, L. I., & Kataoka, A. 2023, in *Protostars and Planets VII*, ed. S. Inutsuka et al. (San Francisco, CA: ASP)

Mori, S., Bai, X.-N., & Okuzumi, S. 2019, *ApJ*, **872**, 98

Moskalenko, I. V., Strong, A. W., Ormes, J. F., & Potgieter, M. S. 2002, *ApJ*, **565**, 280

Nelson, R. P., Gressel, O., & Umurhan, O. M. 2013, *MNRAS*, **435**, 2610

Notsu, S., van Dishoeck, E. F., Walsh, C., Bosman, A. D., & Nomura, H. 2021, *A&A*, **650**, A180

Öberg, K. I., Boogert, A. C. A., Pontoppidan, K. M., et al. 2011, *ApJ*, **740**, 109

Öberg, K. I., Qi, C., Wilner, D. J., & Andrews, S. M. 2011, *ApJ*, **743**, 152

Padovani, M., Hennebelle, P., Marcowith, A., & Ferrière, K. 2015, *AAP*, **582**, L13

Padovani, M., Marcowith, A., Hennebelle, P., & Ferrière, K. 2016, *AAP*, **590**, A8

Pinte, C., Padgett, D. L., Ménard, F., et al. 2008, *A&A*, **489**, 633

Price, E. M., Cleeves, L. I., & Öberg, K. I. 2020, *ApJ*, **890**, 154

Qi, C., Öberg, K. I., Espaillat, C. C., et al. 2019, *ApJ*, **882**, 160

Qi, C., Öberg, K. I., Wilner, D. J., et al. 2013, *Sci*, **341**, 630

Rab, C., Güdel, M., Padovani, M., et al. 2017, *A&A*, **603**, A96

Schöier, F. L., van der Tak, F. F. S., van Dishoeck, E. F., & Black, J. H. 2005, *A&A*, **432**, 369

Seifert, R. A., Cleeves, L. I., Adams, F. C., & Li, Z.-Y. 2021, *ApJ*, **912**, 136

Simon, J. B., Bai, X.-N., Armitage, P. J., Stone, J. M., & Beckwith, K. 2013a, *ApJ*, **775**, 73

Simon, J. B., Bai, X.-N., Stone, J. M., Armitage, P. J., & Beckwith, K. 2013b, *ApJ*, **764**, 66

Simon, J. B., Lesur, G., Kunz, M. W., & Armitage, P. J. 2015, *MNRAS*, **454**, 1117

Simon, M., Dutrey, A., & Guilloteau, S. 2000, *ApJ*, **545**, 1034

Teague, R. 2019, *JOSS*, **4**, 1632

Teague, R. 2020, *Richteague/keplerian_mask*: Initial Release, v1.0, Zenodo, doi:10.5281/zenodo.4321137

Teague, R., & Foreman-Mackey, D. 2018, *RNAAS*, **2**, 173

Teague, R., Semenov, D., Guilloteau, S., et al. 2015, *A&A*, **574**, A137

Tielens, A. G. G. M., & Hagen, W. 1982, *AAP*, **114**, 245

Umurhan, O. M., Estrada, P. R., & Cuzzi, J. N. 2020, *ApJ*, **895**, 4

Vacca, W. D., & Sandell, G. 2011, *ApJ*, **732**, 8

van der Tak, F. F. S., Black, J. H., Schöier, F. L., Jansen, D. J., & van Dishoeck, E. F. 2007, *A&A*, **468**, 627

van Dishoeck, E. F., Herbst, E., & Neufeld, D. A. 2013, *ChRv*, **113**, 9043

Waggoner, A. R., & Cleeves, L. I. 2022, *ApJ*, **928**, 46

Waggoner, A. R., Cleeves, L. I., Loomis, R. A., et al. 2023, *ApJ*, **956**, 103

Webber, W. R. 1998, *ApJ*, **506**, 329

Whipple, F. L. 1972, in *Proc. 21st Nobel Symposium: From Plasma to Planet*, ed. A. Elvius (New York: Wiley), 211

Yang, C.-C., Mac Low, M.-M., & Johansen, A. 2018, *ApJ*, **868**, 27

Yoshida, T. C., Nomura, H., Furuya, K., Tsukagoshi, T., & Lee, S. 2022, *ApJ*, **932**, 126

Youdin, A. N., & Goodman, J. 2005, *ApJ*, **620**, 459

Zhang, K., Bergin, E. A., Schwarz, K., Krijt, S., & Ciesla, F. 2019, *ApJ*, **883**, 98

Zhang, S., Zhu, Z., Huang, J., et al. 2018, *ApJ*, **869**, L47